Turbulent Axial Odometer Model

Michael E. Olsen*
NASA Ames Research Center, Moffett Field, CA 94035

Randolph P. Lillard[†]
NASA Johnson Space Center, Houston, TX 77058

A Galilean-invariant field equation is proposed and tested on standard turbulence model test cases. The field equation provides an additional non-dimensional outer scale which allows the turbulence models to reproduce the axial normal stress increase with Re_θ seen in high Reynolds numbers experiments. The field equation provides a Reynolds number for every point based on the length of turbulent flow upstream of that point in the domain. This outer scale equation can be considered an odometer that gives a length scale conjectured to be related to the large streamwise structures that are seen in turbulent flow and that require run length to develop. A new RANS model using this additional scale is able to match the Reynolds number variation of the normal stresses seen at high Reynolds number. Furthermore, the good attached flow prediction capabilities of current RANS models appears to be attained. Using this scale equation, the entire Reynolds-stress state appears to be predicted correctly, over a large run length Reynolds number range such as experienced in aircraft design.

I. Nomenclature

List of Symbols

$\overline{u_i}$	ensemble mean velocity in i direction
u_i'	perturbation velocity in i direction, $u_i - \overline{u_i}$
k	turbulent kinetic energy, $\frac{1}{2}\overline{\rho u_i' u_i'}$
ν_T	kinematic eddy viscosity
ε	homogeneous turbulent dissipation
R_{ij}	second moment velocity tensor (Reynolds-stress), $\overline{u_i' u_j'}$
T_{ijk}	third moment velocity tensor, $\overline{u_i' u_j' u_k'}$
Q_{ijkl}	fourth moment velocity tensor, $\overline{u_i' u_j' u_k' u_l'}$
R_o	outer scale variable
R_T	turbulent Reynolds number, $k^2/\nu\varepsilon$
Re_L	run length Reynolds number based on distance L, $u_\infty L/\nu_\infty$
L	flat plate total length
c	airfoil chord
x	axial distance, tensor index 1
y	spanwise distance, tensor index 2
z	wall normal distance, tensor index 3
l_p	turbulent run length
u_∞	free stream velocity
T_∞	free stream static temperature (K)
a_∞	free stream isentropic speed of sound
M_∞	free stream Mach number, $\frac{u_\infty}{a_\infty}$
τ_w	wall shear, $\mu\partial_z u|_w$
ψ	turbulent normal stress difference
Ψ_L	turbulent normal stress difference minimum

*Research Scientist, N230-2, Moffett Field CA 94035-1000, Associate Fellow AIAA
[†]Research Scientist, Johnson Space Center, Houston TX 77058

Ψ_R	turbulent normal stress difference slope
A_6	turbulent time scale ratio (log layer nominal $2S_{13}/\omega$)
α	Wilcox dissipation parameter
R_{NN}	wall normal normal stress parameter
R_m	characteristic odometer Reynolds number parameter
$\mathcal{K}$	log layer (design) TKE in wall units
β^*	dissipation parameter ($= \varepsilon\omega/k$)
β	isotropic decay parameter
n_D	isotropic decay rate (β^*/β)
A_8	Von Karman constant adjustment parameter
σ_ω	turbulent frequency gradient diffusion Prandtl number
σ_t	triple product gradient diffusion Prandtl number
σ_k	turbulent kinetic energy gradient diffusion Prandtl number
σ_r	Reynolds-stress gradient diffusion Prandtl number
R_{11}^+	axial normal Reynolds-stress
R_{33}^+	wall-normal normal Reynolds-stress
R_{22}^+	spanwise normal Reynolds-stress
R_{13}^+	Reynolds shear stress
u_τ	friction velocity, $\sqrt{\tau_w/\rho}$
x_3^+	wall normal distance in wall units, $u_\tau z/\nu$
ν	kinematic viscosity, μ/ρ
μ	molecular viscosity
ρ	mass density

List of Subscripts

∞	freestream (farfield) conditions
w	evaluated at wall

II. Introduction

Reynolds Averaged Navier-Stokes (RANS) Reynolds-stress modeling has a long history, but at the present time simpler eddy viscosity models using the Boussinesq assumption are still the primary method for turbulent flowfield predictions for flowfield predictions. At the turn of the twenty-first century, advances in experimental technique provided new insight into the nature of the Reynolds-stress tensor. While the shear stress and wall normal Reynolds-stress seem to be characterized by the wall units ($u_\tau = \sqrt{\tau_w/\rho}$), the axial ($R_{11}^+$) and spanwise ($R_{22}^+$) normal Reynolds stresses are not constant in wall units, but increase with increasing Re_θ [1–8]. This creates a conundrum in a standard RANS model, as the scaling is on an "outer scale" (Re_θ), and not the wall scaling, u_τ and wall distance. The relatively recent discovery of very large elongated structures in turbulent boundary layers has been proposed as a cause [8].

For attached flows, accurate normal stress estimates are not required to obtain accurate pressure and skin friction predictions, as evidenced by the performance of eddy-viscosity models. However, in separated flows, the inaccurate normal stress are believed to be part of the cause of the poor predictions for reattachment in separated flows [9–11], along with poor predictions of the turbulent transport. Furthermore, for almost any model of turbulent transport, poor estimates of R_{ij} components will lead to incorrect turbulent transport ($\partial_k T_{ijk}$) estimates.

Based on this need for an outer length scale, a new field equation has been developed. The equation is designed to provide a non-dimensional quantity that is a Reynolds number formed by the length of streamlines continuously inside turbulent flow, the square root of the turbulent kinetic energy, and the molecular velocity ($\sqrt{k}l_p/\nu$). The equation is Galilean invariant, and when coupled with a modified version of the triple product model [12] provides a reasonable estimate of the axial Reynolds stress variations seen in experiment [4, 6–8]—something that no other current turbulence model is capable of.

A. TAO field equation description

As a novel field equation is proposed here, a quick look at the conceptual origin, properties, and solutions of this new field equation is in order. The equation is claimed to be Galilean-invariant (a primary requirement for anything claiming to be a physical law at non-relativistic speeds), so there should be a physical entity whose properties do not depend on the coordinate system involved. In this case, the underlying reality is a streamline length. Essentially, the field equation acts like an odometer which increases as long as the streamline remains within a turbulent field, hence the name—Turbulent Axial Odometer (TAO). One further design decision in this field equation is that "odometers" along adjacent streamlines should synchronize themselves (with a gradient diffusion term) so that all odometers within a turbulent boundary layer should yield roughly the same length (or scale) estimate at the same axial location. A final design decision in crafting this equation, one that fits with its characterization as an odometer, is that the field variable (odometer reading) should reset itself towards zero when the streamline is no longer in a turbulent region.

B. Building a Field Equation Odometer

Let us start by considering an equation that should give a running distance along a streamline (l_p) Eq. (1a),

$$\rho \partial_t(l_p) + \rho u_i \partial_i(l_p) = \rho(u_i u_i)^{\frac{1}{2}} \tag{1a}$$

That this equation has this property can seen by considering steady uniform flow, and simplifying,

$$\rho u_i \partial_i(l_p) = \rho(u_i u_i)^{\frac{1}{2}}$$

which implies, for axial flow, say in the x_1 direction

$$\partial_1(l_p) = 1$$

and integrating

$$l_p = x_1$$

where x_1 is assumed to be zero at the start of the streamline. By integrating this equation (essentially by a method of characteristics) from the outer boundaries into the interior of the flowfield, the value of l_p will simply give the arclength of the streamline through that point in space from the point of origin at the inflow boundary. So now, we have a field equation that has a field variable equal to the length of the streamline from the boundary inflow point of the streamline to that point—an odometer.

The next step is to take this simple result and bend it to the purpose of obtaining an outer scale. This outer scale needs, for our purposes, to be a non-dimensional number, and multiplying l_p by $\sqrt{k}/\nu$ leaps to mind. For a flat plate, k is very nearly constant in the log layer, and very small away from it. In general, in thin shear layer flows, the central shear region is the only place where k is appreciable, and outside of this region k is small and decreasing along streamlines, since there is no production and turbulent dissipation continues to turn k into increased internal energy.

$$\partial_t(\rho R_o) + \partial_i(\rho u_i R_o) = \rho \sqrt{u_i u_i} \frac{\sqrt{k}}{\nu} \tag{1b}$$

At this point, the equation is purely hyperbolic, and provides a non-dimensional Reynolds number whose length is the streamline length weighted by $\sqrt{k}/\nu$. The next term to be added is a diffusion term to synchronize the odometers of adjacent streamlines so that in a wall bounded shear layer the odometer values are consistent across the entire boundary layer at that axial location.

$$\partial_t(\rho R_o) + \partial_i(\rho u_i R_o) = \rho \frac{\sqrt{u_i u_i} \sqrt{k}}{\nu} + \partial_i \left((\mu + \sigma_t \mu_t) \partial_i R_o \right) \tag{1c}$$

After some experimentation, this non-dimensional variable seemed to be viable as an option, allowing a reasonable match of the normal stress anisotropy variations in the flat plate when used as part of a turbulence model. However,

further experimentation on separated flows made the need for a destruction term apparent. To accomplish this, a destruction (odometer reset) term was added to the field equation, $-\omega R_o/(1 + R_T)$, which causes the R_o term to reset itself to zero if the streamline leaves turbulent flow (which is characterized by high R_T).

$$\partial_t(\rho R_o) + \partial_i(\rho u_i R_o) = \rho \frac{\sqrt{u_i u_i}\sqrt{k}}{\nu} + \partial_i\left((\mu + \sigma_t \mu_t)\partial_i R_o\right) - \frac{\rho \omega R_o}{(1 + R_T)} \tag{1d}$$

The R_o variable is determined by Eq. (2), the new equation for the outer scale :

$$\partial_t(\rho R_o) + \partial_i(\rho u_i R_o) = \rho \frac{\sqrt{u_i u_i}\sqrt{k}}{\nu} + \partial_i\left((\mu + \sigma_t \mu_t)\partial_i R_o\right) - \frac{\rho \omega R_o}{(1 + R_T)} \tag{2}$$

The boundary conditions for this equation are that at inflow boundaries, R_o is zero, and at walls $\partial_n R_o = 0$. Outflow boundary conditions are simple extrapolation.

The field variable from this equation (R_o) is used to adjust the field equations of the associated turbulence model (see Section III) to match the experimental variation of the normal axial Reynolds-stress. Note that this equation uses the values of k, ν_T and R_T from the underlying turbulence model, which have predictable functional forms for most thin shear layer flows. This means that as long as the model consistently gives correct estimates of these variables, the R_o returned from this equation is relatively model-independent for models that consistently predict k, ν_T, and R_T .

C. Odometer Solutions

Before showing the results of the odometer-enhanced turbulence model, we will show the character of the solutions of the R_o equation itself for two representative flowfields. The first flowfield discussed is, naturally enough, the flat plate.
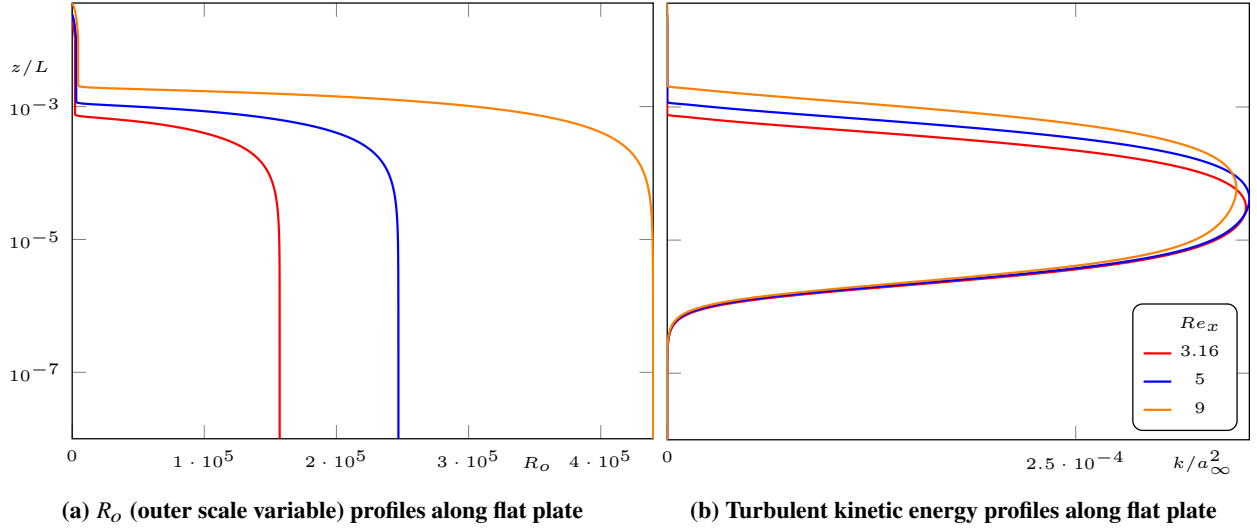
1. Flat Plate

(a) R_o (outer scale variable) profiles along flat plate   (b) Turbulent kinetic energy profiles along flat plate

Fig. 1   Boundary layer profiles of k and R_o for the flat plate

Profiles of the solutions of the scale equation, R_o, are shown in Fig. 1a. The corresponding k profiles are shown in Fig. 1b. The k profiles give an indication where the turbulent flow is in this flowfield—close to the wall. The R_o profiles are flat in the corresponding region, and drop to small values away from the wall where the streamlines do not enter the region of turbulent flow.

The R_o solutions have the desired character—from the edge of the turbulent region to the wall, R_o is very nearly constant. In the region outside the turbulent wall region, the R_o is very small. Looking at the value of R_o in the turbulent region at the three axial locations plotted in Fig. 1a, R_o does roughly scale with the run length—again consistent with

the design of the outer scale equation. For this particular boundary value problem, the run length of the streamline inside the turbulent region can be easily estimated and the equation for R_o is working exactly as intended.

However, the utility of this field equation will require that it act in a similar manner on far more complex configurations. The next flowfield to be shown here gives an idea of how the model would work on flowfields more representative of those encountered in actual aerospace vehicle design or analysis.

D. Isolated Airfoil: NACA 4412

(a) $10c$ **outer boundary**

(b) $100c$ **outer boundary**
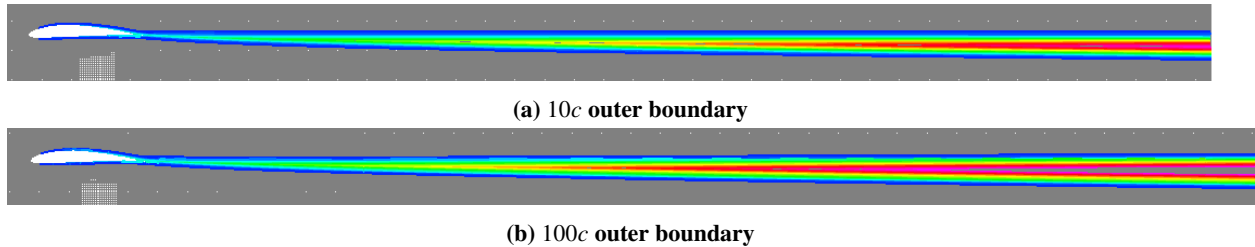
Fig. 2 R_o solution on 2D airfoil

(a) R_o **(outer scale variable)**
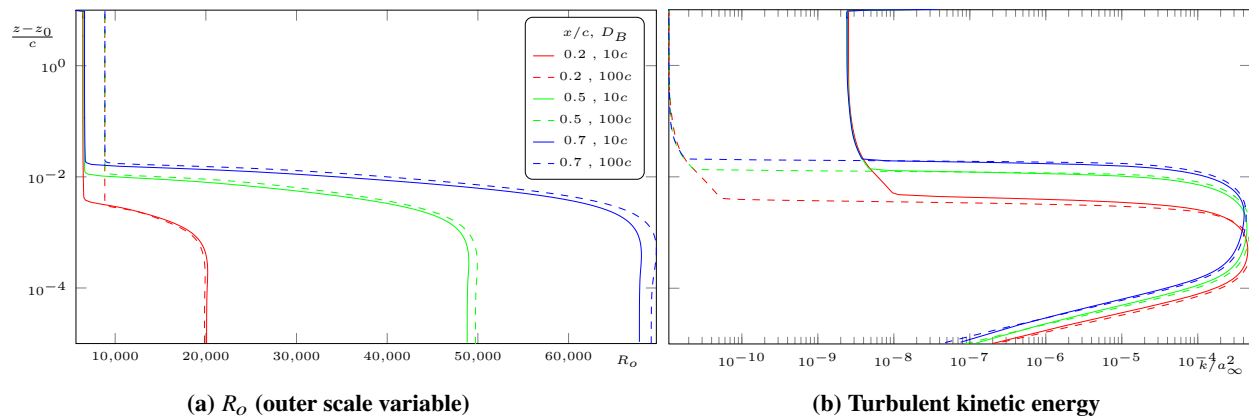
(b) **Turbulent kinetic energy**

Fig. 3   Boundary layer profiles at three x/c locations for the airfoil, (D_B is farfield boundary distance)

The freestream chord Reynolds number for this particular solution is $u_\infty c/\nu_\infty = 1.5 \times 10^6$, and the freestream Mach number is 0.2. However, this flowfield has external boundaries far from the turbulent wall bounded field. The same set of boundary conditions described above for the flat plate are used for the airfoil. On inflow faces, R_o is set to zero ($R_o = 0$). At outflow boundaries, simple extrapolation is used. At walls, the wall normal derivative of R_o is set to zero ($\partial_n R_o = 0$).

The behavior of k in the underlying model, which is tuned to match the decay of isotropic turbulence, ensures that k starts out small and gets smaller as the flow traverses the streamline in the absence of mean strain. For this case, solutions obtained on two different grid systems are compared to assess the sensitivity of the model predictions to large fractions of the streamline length traversing non-turbulent flow before it reaches the wall bounded turbulent shear layer. One grid system has external boundaries ten chords away from the airfoil and the other has those boundaries one hundred chords away.

Figure 2 shows the contours of R_o of these two solutions, with most of the external regions trimmed away. As can be seen, even though the $100c$ solution has much further upstream length for streamlines to reach the airfoil, the R_o values look very similar, and the regions upstream and away from the turbulent region are regions of small R_o, exactly as one would want. In the flowfield where laminar k is small, the outer scale is small. However, near the airfoil where the flow becomes turbulent near the wall, and in the wake behind the airfoil, the outer scale variable R_o grows with greater run length.

While the color contours of R_o give a first order assessment of the nature of the solution, it is more instructive to look at the profiles of R_o over the airfoil. Looking in detail at the upper surface of the airfoil, boundary layer profiles of

5

the outer scale variable, R_o, are shown in Fig. 3. The R_o profiles (Fig. 3a) are acting in the manner they were designed to act—nearly constant within the boundary layer, and dropping to a small number in the outer flowfield. Furthermore, the R_o solutions are essentially insensitive to the change in external boundary distances.

The corresponding profiles for k (Fig. 3b) are what one might expect, with small differences in the boundary layer width (more noticeable for smaller x/c) but essentially the same k levels in the wall bounded flow even though the external k levels are substantially different (though both extremely small). In short, the solutions look very much like the corresponding solution on the flat plate flowfield, and provide the same sort of run length scaling even when the starting point of the streamlines is a hundred chords away. Solutions on other more complicated flowfields confirm that the new field equation is a reasonable outer scale that measures the run length of turbulent flow, weighted by the variable $\sqrt{k}$ which is well correlated to u_τ for attached flowfields.

III. Methodology and Turbulence Model Description

This section discusses the details of the solution method used and the overall TAO enhanced turbulence model. The solution methodology is unchanged from previous work, and the model can be characterized as very similar to previous Lag-T_{ijk} models, with the important addition of the outer scale R_o to adjust model parameters to match the variations of the Reynolds-stress tensor observed experimentally.

A. Computation

1. Grid

The flat plate grid used (Fig. 4) is 513×513, with initial wall normal spacing of $10^{-8}L$ and an initial axial spacing of $10^{-4}L$. The wall normal stretching ratio is less that 1.03, and the axial stretching ratio is less that 1.02. The grid vertical extent starts at the leading edge at $0.01L$, and linearly grows to $0.3L$ at the trailing edge, very similar to grids from [10]. The grid is sufficiently fine to allow simulation of this flowfield at axial locations that are less than $0.005L$, which corresponds to a Reynolds number based on run distance and freestream velocity of 500×10^3, nominally the lowest Reynolds number at which it would be possible to have turbulent flow at normal conditions.

2. Boundary Value Problem Definition

The primary flowfield to be studied is the canonical low Mach number turbulent flat plate. This simulation has a Reynolds number based on plate length and freestream velocity of 100×10^6, which gives a long region of fully developed turbulent flow—certainly 90% of the plate length. The simulation Mach number was set to 0.2, yielding an essentially incompressible flow field without requiring low Mach preconditioning.

The boundary conditions on the plate are viscous, adiabatic wall along $z = 0$, characteristic boundary conditions along the inflow plane and upper edge, and simple extrapolation along the exit plane. A detail that is generally not discussed at any length is the freestream conditions for k and $R_T = \frac{k}{\nu\omega}$. The standard conditions used are to set $k_\infty = 1 \times 10^{-6}$, and $Re_T = 0.1$, which is essentially laminar freestream. The turbulent kinetic energy continues to decay from the inflow edge, and k and Re_T are actually lower for any part of the solution domain without significant shear strain. This can be thought of as "Flight" conditions, where the atmospheric turbulence is vanishingly small, and this is the usual boundary condition imposed.

An alternative is to attempt to match the turbulence state existing in a wind tunnel test section, where the grid turbulence of the last screens in the settling chamber is accelerated through the contraction section, then traverses down the tunnel at a nearly constant freestream turbulence intensity. This is done by setting k to the desired level, and $Re_T \geq 1000$. If a measurement of the decay of k down the test section is available, this can be used to fix Re_T, but in this paper it is set to 1000 for the cases where non-zero freestream turbulence is being simulated. This value gives a nearly constant freestream k over the length of the plate. Choosing higher levels of Re_T gives results that are essentially similar. Setting the freestream turbulent state in this manner is denoted as "Wind Tunnel" turbulence levels. For this paper, the standard "Flight" turbulence level boundary values are used.

3. Numerical Method

The code used in this study was a modified version of OVERFLOW 2.2k [13, 14]. The modifications included the addition of Lag, Lag-R_{ij}, and TTR models along with the high speed modifications [15]. Matrix dissipation was used

with smoothing parameters as recommended by earlier studies of high-speed flows with this code [15] with one critical change. The critical difference in the matrix dissipation smoothing parameters used is that the eigenvalue limiters are set to zero. Matrix dissipation [16] is appropriate for this flowfield.

The Pulliam-Chaussee diagonal scheme [17], with variable time stepping or a constant Courant number (CFL) and multigrid was used as the relaxation method. Grid sequencing (called full multigrid in OVERFLOW) was utilized, and allowed a check on grid convergence as well as drastically reducing the CPU time required to fully converge the results.

Spatial convective terms and diffusion terms were all second-order accurate. For the modeling of the convection terms of the turbulence models, second-order upwind was used on all the RANS models. The Lag methodology does require second-order accuracy (or better) since the field equations defining the lagged turbulent variables are a balance of convection and source with no diffusion terms by design—purely hyperbolic equations to accurately mimic the history effects so clearly evident in turbulent flow. In the turbulent transport level equations, not all the equations are purely hyperbolic, but they are all more driven by convection terms than standard one- or two-equation models.

B. Turbulence Model Description

The scale equation has been incorporated into the equation system of R_{ij}, T_{ijk}, and Q_{ijkl} models. These models are based on the T_{ijk} models described in [11]. Adaptive mesh refinement similar to that described in [18] is used to eliminate the possibility of truncation error adulterating the solutions used to tune the turbulence models.

The remainder of the model definition follows the previous TTR and Reynolds stress development closely [10, 12, 19–21] The TAO turbulence model including turbulent transport (T_{ijk}) terms is:

$$\partial_t (\rho k) + \partial_l (\rho u_l k) = \rho \left[R_{ij} S_{ij} - \beta^* k\omega \right] + \partial_l ((\mu + \sigma_k \mu_T) \partial_l k) - A_4 \partial_l (\rho T_{iil}) \tag{3a}$$

$$\partial_t (\rho \omega) + \partial_l (\rho u_l \omega) = \alpha \rho S^2 - \beta \rho \omega^2 + \partial_l ((\mu + \sigma_\omega \mu_T) \partial_l \omega) \tag{3b}$$

$$\partial_t (\rho R_{ij}) + \partial_l (\rho u_l R_{ij}) = A_0 \rho \omega \left(R_{ij}^{(eq)} - R_{ij} \right) \tag{3c}$$

$$\partial_t (\rho T_{ijk}) + \partial_l (\rho u_l T_{ijk}) = A_0 \rho \omega \left(T_{ijk}^{(eq)} - T_{ijk} \right) \tag{3d}$$

where

$$
T_{ijk}^{(eq)} = \frac{A_2}{A_0 \omega} \left[T_{ijl} \partial_l \overline{U_k} + T_{jkl} \partial_l \overline{U_i} + T_{kil} \partial_l \overline{U_j} - R_{ij} \partial_l R_{kl} - R_{jk} \partial_l R_{il} - R_{ki} \partial_l R_{jl} \right]
$$
$$
+ \frac{1}{A_0 \rho \omega} \left[\partial_l \left((\mu + \sigma_t \mu_{t_E}) \partial_l T_{ijk} \right) \right] \tag{4}
$$

$$\mu_{t_E} = \rho k / \omega \qquad\qquad S = \sqrt{2 \left(S_{ij} S_{ij} - S_{kk}^2/3 \right)}$$

$$\overline{\mathcal{P}} = R_{ij} S_{ij}$$

$$\varepsilon = \beta^* k\omega \qquad\qquad S_{ij} = \frac{1}{2} \left(\frac{\partial u_i}{\partial x_j} + \frac{\partial u_j}{\partial x_i} \right)$$

Most of the parameters for this model are set by the requirement to retain the equilibrium predictions of the underlying k-ω 1988 model. The equilibrium Reynolds-stress relation is one of the three described in earlier Reynolds-stress model work [21], denoted as the "926(Redistribution)" Equilibrium Reynolds-stress relation. This constitutive relation is most directly related to the explicit algebraic Reynolds-stress models [22–24]. The terminology is borrowed from the paper introducing this relation [21], and contains production terms which are *not* the full Reynolds-stress production terms, but do yield log layer anisotropies consistent with the classic 4:3:2 [25] relation for a constant structure parameter $A_1 = \frac{5}{3}$. These "production" terms (which are actually only redistribution terms, and none of the work terms of actual production) are

$$\mathcal{P}_{11} = 2 \left(k S_{11}/A_1 + (R_{31} \Omega_{31} - R_{12} \Omega_{12}) \right) \tag{5a}$$

$$\mathcal{P}_{22} = 2 \left(k S_{22}/A_1 + (R_{12} \Omega_{12} - R_{23} \Omega_{23}) \right) \tag{5b}$$

$$\mathcal{P}_{33} = 2 \left(k S_{33}/A_1 + (R_{23} \Omega_{23} - R_{31} \Omega_{31}) \right) \tag{5c}$$

7

with corresponding off-diagonal terms

$$\mathcal{P}_{12} = 2kS_{12}/A_1 + (R_{23}\Omega_{31} - R_{31}\Omega_{23} + (R_{11} - R_{22})\Omega_{12}) \tag{5d}$$

$$\mathcal{P}_{23} = 2kS_{23}/A_1 + (R_{31}\Omega_{12} - R_{12}\Omega_{31} + (R_{22} - R_{33})\Omega_{23}) \tag{5e}$$

$$\mathcal{P}_{31} = 2kS_{31}/A_1 + (R_{12}\Omega_{23} - R_{23}\Omega_{12} + (R_{33} - R_{11})\Omega_{31}) \tag{5f}$$

then the equilibrium Reynolds stress is given by:

$$R_{ij}{}^{(eq)} = \frac{2}{3}k\delta_{ij} - \frac{A_1}{\omega}(\mathcal{P}_{ij} - \frac{1}{3}\overline{\mathcal{P}}\delta_{ij}) + \frac{\partial_l\left((\mu + \sigma_r\mu_T)\partial_l R_{ij}\right) - A_3\partial_l\left(\rho T_{ijl}\right)}{A_0\rho\omega} \tag{6}$$

The model parameters which are constant for the TAO model in this paper is:

$A_0 = 1.0$	$A_2 = 1.0$	$A_3 = 1.0$	$A_4 = 1.0$
$\sigma_k = 0.3$	$\sigma_r = 1.0$	$\sigma_t = 1.0$	$\alpha = 0.04$
$R_m = 10.0$	$A_8 = 0.6$	$n_D = 1.2$	$\Psi_L = 0.5$
$\Psi_R = 0.1$			

In order to provide the needed adjustments to match R_{11}^+, in contrast to the previous triple product models, this model has a variable $A_1(R_o)$, which is provided by the following functional system:

$$\psi = \max(\Psi_L, \Psi_R \ln(1 + R_o/R_m)) \tag{7a}$$

$$A_6 = \frac{2}{3}\frac{1 + \psi^2}{R_{NN} + \psi} \tag{7b}$$

$$A_1 = \psi/A_6 \tag{7c}$$

$$\mathcal{K} = \frac{1 + \psi^2}{A_6} \tag{7d}$$

$$\beta^* = \psi/A_6 \tag{7e}$$

$$\beta = \beta^*/n_D \tag{7f}$$

$$\sigma_\omega = \frac{\beta/A_6^2 - \alpha}{\mathcal{K}A_8^2} \tag{7g}$$

This functional system (arrived at by an extension of Wilcox's analysis [26, 27] for eddy viscosity models) provides a framework where the adjustments are more clearly identified. ψ is roughly the value of R_{11}^+ -R_{33}^+ in the log layer of a flat plate. R_{NN} (which is a constant parameter in this version) controls the value of R_{33}^+ in the log layer. A_6 is the ratio of the mean strain rate and ω (which is constant in the previous models and the underlying k-ω_{88} model. In order to obtain R_{33}^+ value that better matches experiment (slightly greater than unity, and not a strong function of run length Reynolds number) and allow R_{11}^+ to grow slowly (but unbounded) with Reynolds number, this additional functional complexity was required. The variables $[A_6, A_8]$ are not actually used in the model other than to provide $[A_1, \beta^*, \beta, \sigma_\omega]$.

IV. Results

A. Flat plate

The initial grid used for assessing the turbulence model parameters is shown in Fig. 4. The freestream conditions are specified as $M_\infty = 0.2$, $Re_L = 100 \times 10^6$, $T_\infty = 300K$, $k_\infty = 100 \times 10^{-6}$, $R_T = 0.1$. Boundary conditions are adiabatic viscous wall, extrapolation on the downstream edge, and characteristic conditions on the upstream outboard and upstream edges. The first point of reference for any turbulence prediction method is whether it can predict the flat plate mean flowfield (Fig. 5). Figure 5b shows the surface shear predictions of the TAO model. The "Fully Turbulent" results have no imposed laminar region; all equations are integrated over the entire plate length. The "Transitioned" results have the turbulence production terms zeroed over the front of the plate up to a run length Reynolds number
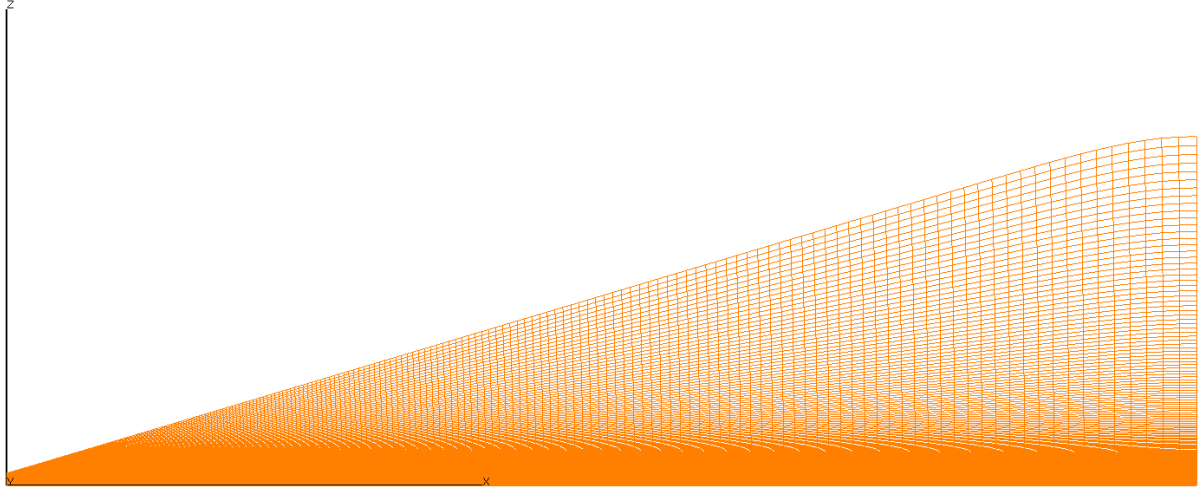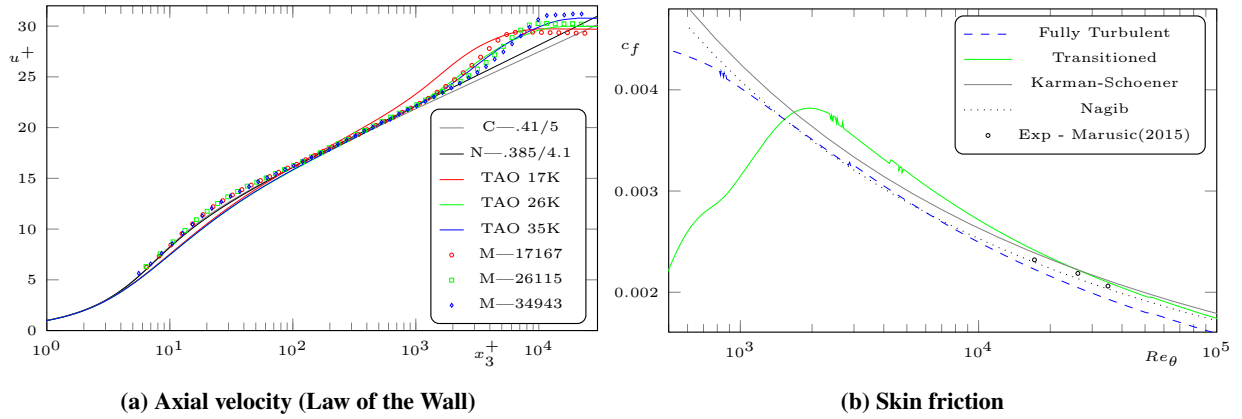
Fig. 4   Flat plate grid system

(a) Axial velocity (Law of the Wall)

(b) Skin friction

Fig. 5   Skin friction and axial velocity predictions (C-Coles version (κ/A), N-Nagib version(κ/A), M-Marusic experiment, Re_θ values for TAO and experiment)

($\rho_\infty u_\infty x/\nu_\infty$) of 200×10^3. The axial velocity predictions are shown in Fig. 5a. These are shown only for the transitional solution, as the fully turbulent results are indistinguishable from the transitional results on this graph.

However, the persistence of differences in c_f between untripped and tripped solutions, and the "transition" behavior of this new model (the blue dashed curve in Fig. 5b, which is still rising up to the "Fully Turbulent" curve at $Re_\theta \approx 500$) are worth noting. The "half measures" turbulence model version [10] had a similar, though more extreme, transitional behavior. This previous model had a high and constant value of R_{11}^+ (≈ 6) in the log layer. It turned out that "Wind Tunnel" freestream turbulence levels had to be imposed at the inflow in order to get the model to be in a fully turbulent state at $Re_x = 1 \times 10^6$. It in effect wanted to act as a combined transition and RANS model. When the TAO model tuning was finished, it did transition (that is, sustain turbulent flow) at $Re_x = 500 \times 10^3$, with "Flight" turbulence levels. At this point, the simulations with an enforced transition look more plausible in the low Reynolds number regime ($Re+_x \leq 2 \times 10^6$) than the "Fully Turbulent" simulations. The differences between predictions of axial velocity (in wall units) at $Re_x \geq 5 \times 10^6$ are miniscule, and the biggest difference is the slight lowering of the wall shear. From this point forward, in the flat plate, only the "Transitioned" results will be shown, although at the Reynolds numbers shown there is no difference visible at the scale of these plots.

The match is the result of model tuning, but it does show that the TAO model is capable of reproducing these results. Essentially, it says that the axial velocity profile, including the slope at the wall, is well predicted. The real point of this new model, prediction of the axial normal Reynolds-stress, is exhibited in Fig. 6. The numbers associated with each curve in the legend are the value of Re_θ for each curve, along with a leading initial denoting the experimental team.
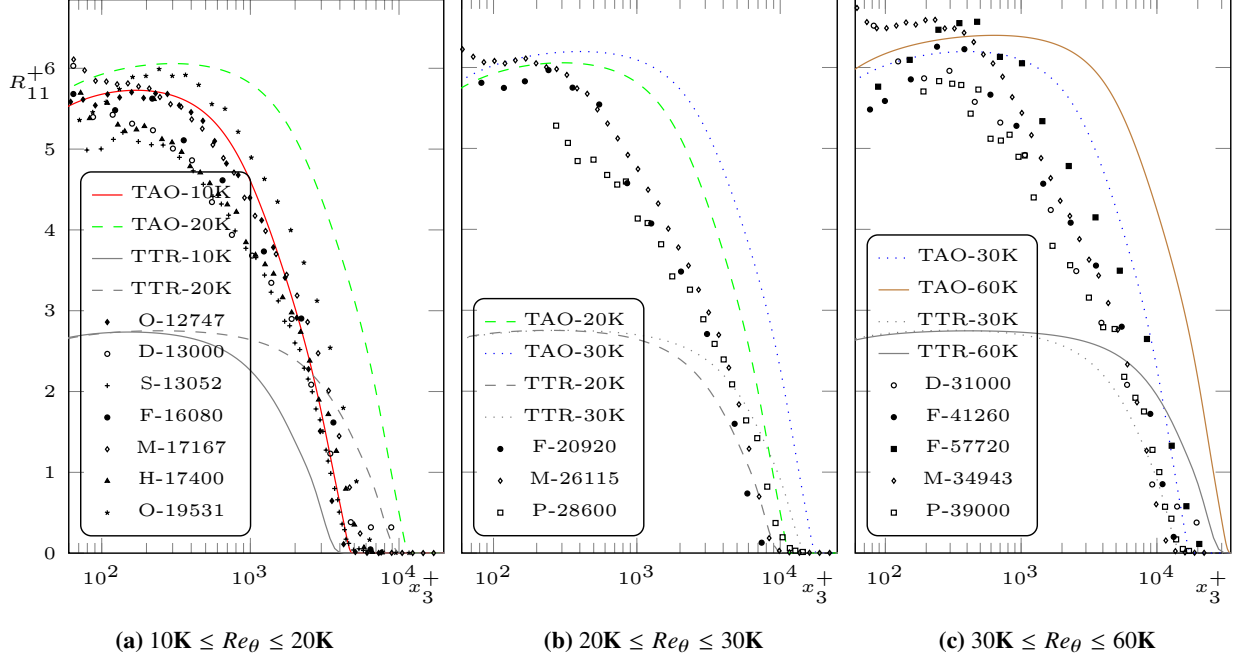
Fig. 6   Axial normal Reynolds-stress Variations (R_{11}^+) compared with experiment (numbers in legend are Re_θ)
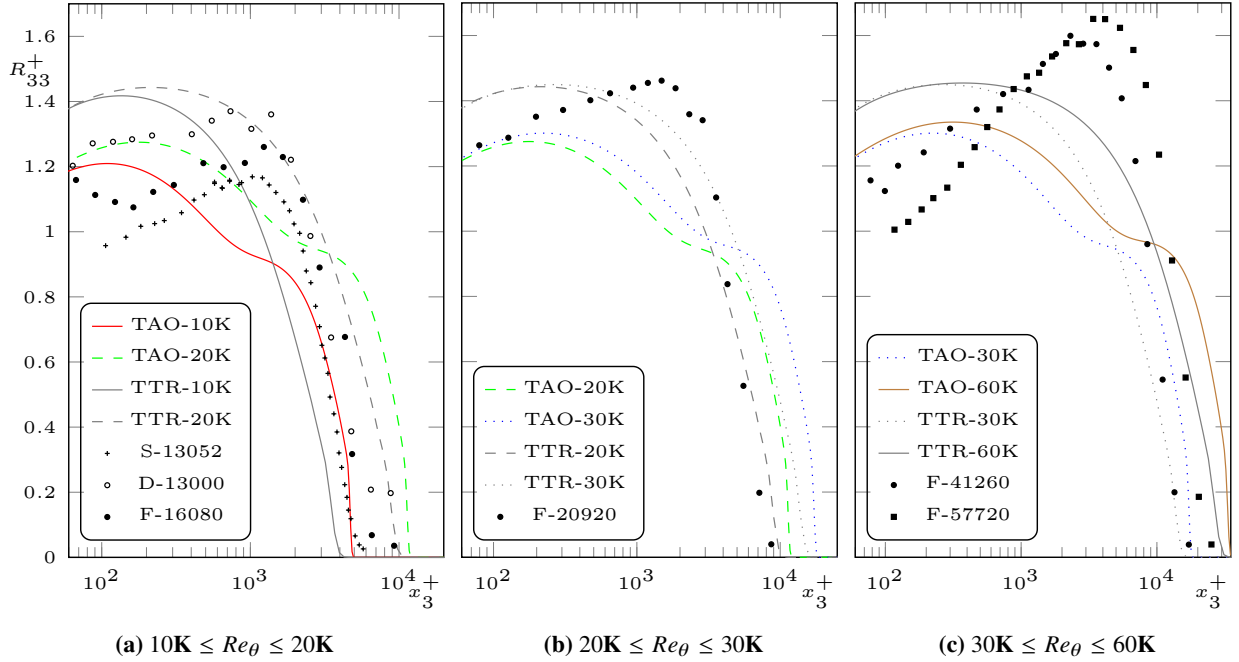

Fig. 7   Wall-normal normal Reynolds-stress (R_{33}^+) Variations compared with experiment

Again, as in the precursor [12], the region of interest is above the viscous sublayer and buffer layer, $z^+ > 60$. Numerous experimental results are shown, parameterized by Re_θ. It is useful to remember that upstream differences can persist in experiment—the work of Marusic et al. [28] is a useful reference when evaluating these predictions. Details of upstream history, such as over-zealous tripping, will affect the outer portion of these profiles, so there is an inherent fuzziness to the outer edge of the Reynolds-stress profiles. As can be seen in the plots, there is also the usual uncertainty in difficult measurement conditions, but the agreement in terms of the inner plateau is generally good. The gray curves

10

on this figure show the results for the TTR model [10], which is representative of a R_{ij} model tuned to provide the classic $4:3:2$ proportions of normal Reynolds-stress in a flat plate boundary layer.

The second improvement made possible by inclusion of the odometer equation is shown in Fig. 7, the wall normal Reynolds stress. The simultaneous improvement in prediction of R_{11}^+ and R_{33}^+ means that the entire Reynolds-stress state in the axial/wall-normal (since the R_{13}^+ is also predicted well given that wall shear is matched Fig. 5b). It is this match of the complete "Mohr's circle" [29] which was the reason for this enhancement to Reynolds-stress modeling.

In the same way that the turbulent transport terms are more important in a separated flow, the entire Reynolds-stress tensor becomes important in a separated flow because there is no well defined flow direction. The difference between R_{11}^+ and R_{33}^+, along with R_{13}^+, determine the maximum shear stress, and its direction, in a separated flow. In the same way that R_{11}^+ was predicted below what it should have been, the R_{33}^+ was predicted too high, and the difference between them was shortchanged on both sides. This means that the predicted maximum shear stress in the separated region could never be as high as it should have been, leading to a decrease in the momentum transfer in the separated region. The grey curves in this figure are again from the TTR model, which is representative of current Reynolds-stress modeling.

While there is still room for improvement in the R_{33}^+ predictions seen in Fig. 7, in the log layer region (where R_{11}^+ is the highest) the R_{11}^+ -R_{33}^+ predictions should be much better predicted in the log region. Another point to keep in mind is that the vertical scale is very different between Fig. 6 and Fig. 7. The maximum discrepancies in R_{33}^+ in Fig. 7 (which are not in the log layer, but out at the boundary layer edge) are below 0.5, which is very small on the scale of Fig. 6.

Along with obtaining a better prediction of the state of stress, better predicted R_{11}^+, R_{33}^+, R_{13}^+ should allow better turbulent transport predictions. Although it is not a dominant term in the turbulent transport for this flow, there are experimental results for one of the triple products, in the form of skewness measurements, $S_u = T_{111}/(R_{11})^{3/2}$. Figure 8 shows a comparison of the predictions for this ratio for the same Re_θ range as the R_{11}^+ and R_{33}^+ plots. It should be kept in mind that there is a discrepancy in "boundary layer edge" of the R_{11}^+ between experiment and computation, so if the "edge" is aligned between experiment and computation, the slope is not badly estimated. It is also interesting that there is a somewhat large δ function spike (at least in the log coordinates of Fig. 8, that is mirrored in the experimental data (see the lowest points on each of the subfigures, which is an experimental minimum). This is a consequence of the balancing process at the far boundary layer edge being turbulent transport matching the convection term which is bringing low turbulence fluid from the freestream into the boundary layer edge.
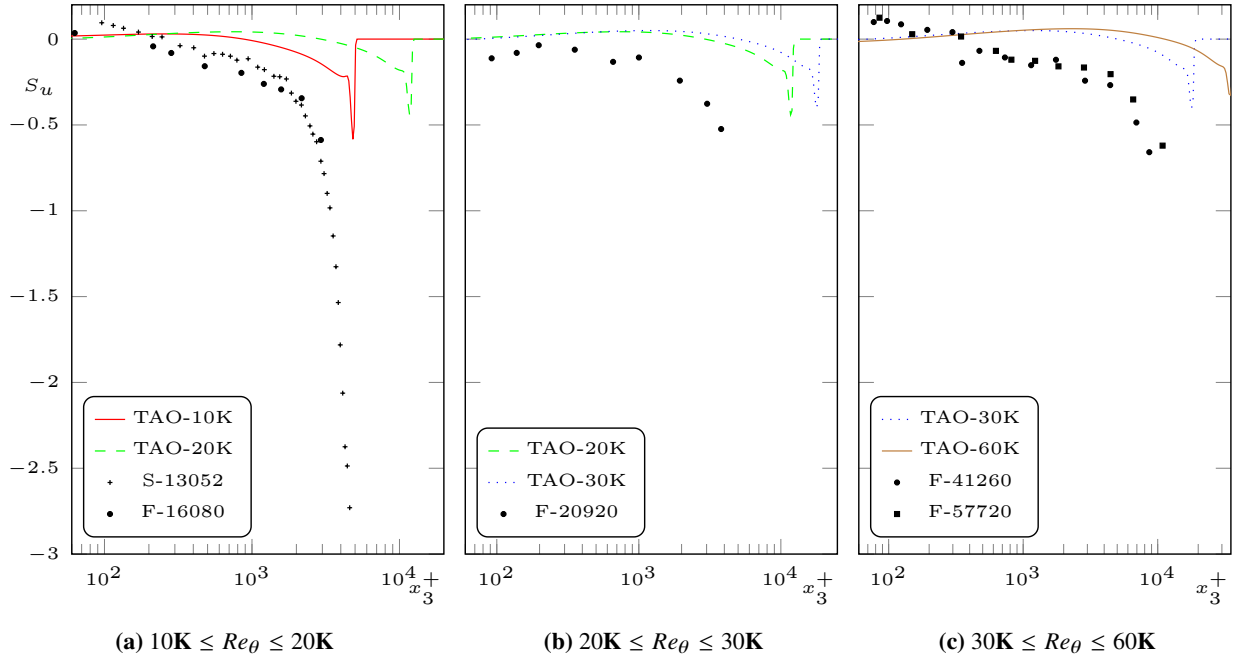

(a) $10\mathbf{K} \leq Re_\theta \leq 20\mathbf{K}$ (b) $20\mathbf{K} \leq Re_\theta \leq 30\mathbf{K}$ (c) $30\mathbf{K} \leq Re_\theta \leq 60\mathbf{K}$

Fig. 8   Skewness ($T_{111}/(R_{11})^{3/2}$) compared with experiment

This can be seen in the final plot to round out the exploration of this new model: the turbulent kinetic energy balance, Fig. 9. These plots extend from deep inside the sublayer to outside the boundary layer edge, shown for three different values of Re_x. The terms are normalized by $u_\tau^3/\kappa x_3^+$, essentially the log layer production. The actual production (green

curve) exceeds this value at all three Re_x, in the log layer (it exceeds unity on this figure when $x_3^+ > 100$). Dissipation (red curve) is much closer to unity in this region, and as one might expect largely balances production. However, as was evident in tuning, the modelled turbulent transport (blue curve), $\partial_k T_{ijk}$ is not negligible in the log layer. By the same token, the gradient diffusion (teal curve), $\nabla(\sigma_k \nabla k)$ is a small but finite term in the log layer. Both are transporting energy out of the log layer into the boundary layer edge and sublayer regions.

As was noted in the earlier, "half measures" paper [10], the place where the triple product term is a balancing one is at the boundary layer edge. In this region, the $\partial_k T_{ijk}$ is balanced by the convection, $\frac{Dk}{Dt}$. Convection (orange curve) is providing lower k fluid into the domain at the boundary layer edge, and the turbulent transport (almost certainly by wall normal transport) is moving high k fluid from the log layer region into the quiescent external flow.
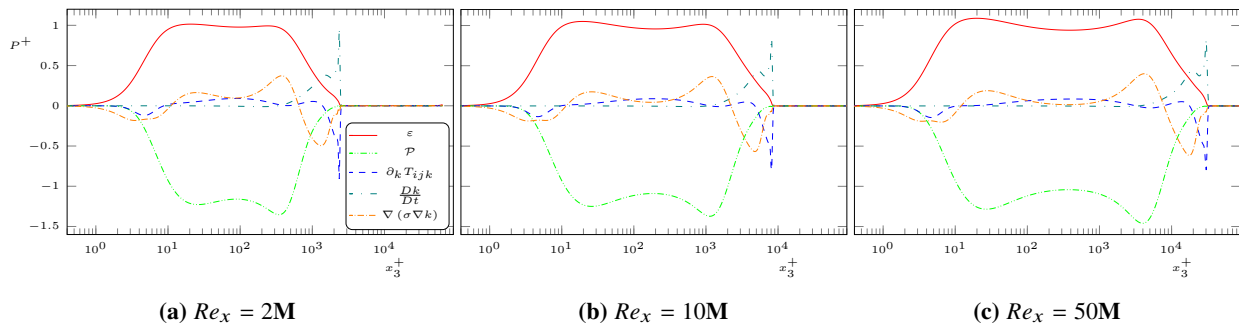

(a) $Re_x = 2$**M** **(b)** $Re_x = 10$**M** **(c)** $Re_x = 50$**M**

Fig. 9   Turbulent kinetic energy balance

V. Conclusions

A new field equation that acts as a turbulence odometer has been coupled with an advanced turbulence model to provide a more accurate prediction of the axial and wall-normal components of the Reynolds-stress tensor. With the proper coupling, the R_{11}^+, R_{33}^+, and R_{13}^+ Reynolds-stress behaviors for flat plate boundary layers are reproduced. Even the somewhat limited triple product comparisons were consistent with experiment.

The new model with the associated new field equation and flow variable have great promise to provide predictions for industry-relevant Reynolds numbers. Comparison on more complex flowfields, especially the junction flow experiment, will enable a possibly large expansion of prediction capability for aircraft design. However, as has been apparent in simulation of canonical flowfields, a much richer validation data set than available in old data sets will be required to allow an unambiguous comparison with experiment.

VI. Future Work

Evaluation of the predictions of the TAO model in attached flow so far suggest that the legacy RANS ability to get good attached flow predictions of c_f was retained, as expected. Additional physics were added to the model predictions—better matching of the full Reynolds-stress tensor, but no harm appears to have been done to one of the more important roles of RANS models, attached flow drag prediction.

Initial separated flow solutions suggest that better matching of the complete Reynolds-stress tensor improves the separation predictions, but also suggest that more complete simulation of the experiment is required. For these models, flow history is more important and simple expedients like adding upstream length to match a boundary layer height are no longer sufficient to match the actual inflow conditions of the experiment. Velocity profiles and Reynolds-stress profiles are both now required to match. However, if this provides the ability to predict flowfields that are industry relevant, it will provide a valuable capability not matched by any other method.

Acknowledgements

References

[1] Petrie, H.L., Fontaine, A.A., Sommer, S. T., and Brungart, T.A., "Large Flat Plate Turbulent Boundary Layer Evaluation," TM 89-207, Penn State Applied Reseach Laboratory, May 18 1990. Technical Memorandum, File No 89-207.

[2] Smith, Randall William, "Effect of Reynolds Number on the Structure of Turbulent Boundary Layers," Ph.D. thesis, Princeton University, January 1994.

[3] Hites, M. H., "Scaling of high-Reynolds number turbulent boundary layers in the National Diagnostic Facility," Ph.D. thesis, Illinois Institute of Technology, 1997.

[4] Österlund, J. M., "Experimental Studies of Zero Pressure-Gradient Turbulent Boundary Layer Flow," Ph.D. thesis, Royal Institute of Technolgy, Stockholm, Sweden, 1999.

[5] DeGraaff, David B., "Reynolds Number Scaling of the Turbulent Boundary Layer on a Flat Plate and on Swept and Unswept Bumps," Ph.D. thesis, Stanford University, January 1999.

[6] De Graaff, David B., and Eaton, John K., "Reynolds-number scaling of the flat-plate turbulent boundary layer," *Journal of Fluid Mechanics*, Vol. 422, 2000, pp. 319–346. doi:10.1017/S0022112000001713, `http://journals.cambridge.org/article_S0022112000001713`.

[7] Marusic, I., McKeon, B. J., Monkewitz, P. A., Nagib, H. M., Smits, A. J., and Sreenivasan, K. R., "Wall-bounded turbulent flows at high Reynolds numbers: Recent advances and key issues," *Physics of Fluids*, Vol. 22, No. 6, 2010, p. 065103. doi:10.1063/1.3453711, URL `https://doi.org/10.1063/1.3453711`.

[8] Smits, A. J., McKeon, B. J., and Marusic, I., "High-Reynolds Number Wall Turbulence," *Annual Review of Fluid Mechanics*, Vol. 43, No. 1, 2011, pp. 353–375. doi:10.1146/annurev-fluid-122109-160753, `http://dx.doi.org/10.1146/annurev-fluid-122109-160753`.

[9] Olsen, M. E., Lillard, R. P., Murman, S. M., Rivers, M. B., Long, K. R., and Ross, J. C., "Separation Prediction of Large Separation with Reynolds Stress Models," *21st AIAA Computational Fluid Dynamics Conference*, 2013, p. 2720. doi:10.2514/6.2013-2720, aIAA Paper 2013-2720,`http://dx.doi.org/10.2514/6.2013-2720`.

[10] Olsen, M. E., "Prediction of Separation with a Third-Order-Moment Model," AIAA Paper 2015-1968`http://dx.doi.org/10.2514/6.2015-1968`, January 2015. doi:10.2514/6.2015-1968.

[11] Olsen, M. E., and Lillard, R. P., "Revised Reynolds-Stress and Triple Product Models," *23rd AIAA Computational Fluid Dynamics Conference*, 2017, p. 3954.

[12] Olsen, M. E., "Reynolds-stress and triple-product models applied to flows with rotation and curvature," AIAA Paper 2016-3942, `http://dx.doi.org/10.2514/6.2016-3942`, Jun 2016. doi:10.2514/6.2016-3942.

[13] Buning, P., Jespersen, D., Pulliam, T., Klopfer, G., Chan, W., Slotnick, J., Krist, S., and Renze, K., *OVERFLOW User's Manual, Version 1.8s*, NASA Langley Research Center, 2000.

[14] Jespersen, D., Pulliam, T., and Buning, P., *Recent enhancements to OVERFLOW*, American Institute of Aeronautics and Astronautics, 1997. doi:10.2514/6.1997-644, aIAA Paper 1997-0664,`http://dx.doi.org/10.2514/6.1997-644`.

[15] Olsen, M., and Prabhu, D., *Application of OVERFLOW to hypersonic perfect gas flowfields*, American Institute of Aeronautics and Astronautics, 2001. doi:10.2514/6.2001-2664, aIAA Paper 2001-2664`http://dx.doi.org/10.2514/6.2001-2664`.

[16] Swanson, R. C., and Turkel, E., "On Central–Difference and Upwind Schemes," *Journal of Computational Physics*, Vol. 101, No. 2, 1992, pp. 292–306. doi:http://dx.doi.org/10.1016/0021-9991(92)90007-L, `http://www.sciencedirect.com/science/article/pii/002199919290007L`.

[17] Pulliam, T., and Chaussee, D., "A diagonal form of an implicit approximate-factorization algorithm," *Journal of Computational Physics*, Vol. 39, No. 2, 1981, pp. 347 – 363. doi:http://dx.doi.org/10.1016/0021-9991(81)90156-X, `http://www.sciencedirect.com/science/article/pii/002199918190156X`.

[18] Olsen, M. E., and Lillard, R. P., "Using Adaptive Mesh Refinement to Study Grid Resolution Effects for Shock-Boundary Layer Interactions," *2018 Fluid Dynamics Conference*, 2018, p. 3858.

[19] Lillard, Randolph, "Turbulence Modeling for Shock Wave/Turbulent Boundary Layer Interactions," Ph.D. thesis, Purdue University, December 2011.

[20] Lillard, R., Oliver, B., Olsen, M., Blaisdell, G., and Lyrintzis, A., "The lagRST Model: a Turbulence Model for Non-Equilibrium Flows," AIAA Paper 2012-0444, `http://dx.doi.org/10.2514/6.2012-444`, Jan 2012. doi:10.2514/6.2012-444.

[21] Olsen, M. E. , Lillard, R. P., and Murman S. M., *Separation Prediction of Large Separation with Reynolds Stress Models*, American Institute of Aeronautics and Astronautics, 2013. doi:10.2514/6.2013-2720, aIAA Paper 2013-2720,`http://dx.doi.org/10.2514/6.2013-2720`.

[22] Pope, S., "A more general effective-viscosity hypothesis," *Journal of Fluid Mechanics*, Vol. 72 (part 2), 1975, pp. 331–340. doi:10.1017/S0022112075003382, `http://journals.cambridge.org/article_S0022112075003382`.

[23] Wallin, Stefan, and Johansson, Arne V., "An explicit algebraic Reynolds stress model for incompressible and compressible turbulent flows," *Journal of Fluid Mechanics*, Vol. 403, 2000, pp. 89–132. doi:10.1017/S0022112099007004, `http://journals.cambridge.org/article_S0022112099007004`.

[24] Hellsten, Antti, "New two equation Turbulence Model for Aerodynamic Applications," Ph.D. thesis, Helsinki University of Technology, February 2004.

[25] Townsend, A.A., *"The structure of turbulent shear flow"*, 2nd ed., Cambridge University Press, 1976.

[26] Wilcox, David C., *Turbulence Modeling for CFD*, DCW Industries, Inc, 1993.

[27] Wilcox, David C., *Turbulence Modeling for CFD*, DCW Industries, Inc, 2006.

[28] Marusic, I., Chauhan, K. A., Kulandaivelu, V., and Hutchins, N., "Evolution of zero-pressure-gradient boundary layers from different tripping conditions," *Journal of Fluid Mechanics*, Vol. 783, 2015, p. 379–411. doi:10.1017/jfm.2015.556.

[29] Wikipedia, "Mohr's Circle," , May 2019. [Online; accessed 16-May-2019]`https://en.wikipedia.org/wiki/Mohr%27s_circle`.